https://doi.org/10.1016/j.jcsr.2022.107679

Behaviour and design of high-strength octagonal CFST short columns subjected to combined compression and bending

Han Fang[1], Qiu-Yun Li[2], Tak-Ming Chan[2*] and **Ben Young[2]**

[1]School of Civil Engineering, University of Leeds, United Kingdom;
[2]Department of Civil and Environmental Engineering, The Hong Kong Polytechnic University, Hong Kong, China;
*Corresponding author: tak-ming.chan@polyu.edu.hk

Abstract

A systematic experimental and numerical investigation on the behaviour of octagonal concrete-filled steel tube short columns fabricated with S690 high-strength steel and C90 high-strength concrete, and subjected to combined compression and bending is reported in this paper. Experiments were firstly performed on twelve short column specimens with different plate width-to-thickness ratios. The experimental results and observations including the ultimate loads, load versus displacement responses and failure modes of the specimens were discussed. In supplementary to the experimental investigation, numerical investigation using a validated finite element model was performed to examine the behaviour of the structures with a wide range of plate width-to-thickness ratios, yield strength of high-strength steel and compressive strength of high-strength concrete that subjected to various combinations of compression and bending. Based on the experimental and numerical results, the applicability of existing design approaches in standards was also evaluated. The assessment shows that the design approaches provide conservative strength predictions for the high-strength octagonal concrete-filled steel tube short columns under combined compression and bending and can be applied to provide safe designs for the structures.

Keywords: Combined compression and bending, Experiments, High-strength concrete, High-strength steel, Numerical modelling, Octagonal concrete-filled steel tube, Structural design.

1. Introduction

Concrete-filled steel tube (CFST) members have gained increasing popularity for the application in the civil infrastructure construction [1-4] since the CFSTs demonstrate enhanced strength and ductility

compared to the steel or reinforced-concrete counterparts due to the composite action between the outer steel tubes and concrete infill. Besides, the CFST members also bring the benefit of faster and economic construction due to the omission of formworks required for constructing reinforced-concrete structures. Over the years, effective research progresses have been made to investigate the behaviour of normal strength CFST members with circular, rectangular, elliptical and octagonal sections [3, 5-12] under realistic loading conditions to obtain reliable design of the structures. Among these cross-sectional shapes, the octagonal CFSTs demonstrate higher strength enhancements from the confinement provided by the octagonal outer tubes than the rectangular CFSTs [12] since the confinement mainly exists at the corners and centre part of the cross-sections and more corner regions for confinement effects are provided within octagonal cross-sections [12-13]. Compared with circular or elliptical CFSTs, the octagonal shape CFST members allow for more flexible connection construction using the flat surfaces of the octagonal cross-sections [12, 14] such as the use of end-plate connections. With these advantages, the octagonal CFST structures have attracted increasing interests from the construction industry and researchers for wide structural applications and were applied as mega-columns for high-rise buildings in China [15].

In addition to the research examining the structural performance of CFSTs with different cross-sectional shapes, increasing research attention has also been paid to high-strength CFST members that are fabricated using high-strength steel (HSS) with nominal yield strength (f_y) above 460MPa and high-strength concrete (HSC) with nominal cylinder compressive strength (f_c) above 70MPa [16-17]. By using these high-strength materials, stronger members with reduced weight consumption of materials can be obtained and generate subsequent savings of energy consumed for transportation and construction of the structural members [18-19]. To take advantage of these benefits, the behaviour of the structures made with high-strength materials needs to be investigated, which can be different from that of the CFST structures fabricated with conventional strength materials due to the higher brittleness of HSC and more susceptibility of HSS tubes to local buckling [20-21]. To address this research need, numerous research studies have been conducted with the primary focus on the behaviour of the members with circular or rectangular sections under compression, bending or combined loadings [9,

21-24]. However, research on the behaviour of high-strength CFST members with octagonal sections that provide high confinement effect from the outer tubes for strength enhancements and ease for connection construction is limited.

Existing research studies on high-strength octagonal CFST members have been limited to short columns subjected to concentric compression. Fang et al. [25] investigated octagonal CFST short columns fabricated using S690 HSS with nominal f_y of 690MPa for the outer octagonal tubes and normal- or high-strength concrete infill with nominal f_c between 50MPa and 90MPa. Short columns with different plate width-to-thickness ratios were tested and investigated numerically through a validated finite element model. It was found that the strength enhancements due to the confinement from outer HSS octagonal tubes and ductility of the structures decreased with increasing plate width-to-thickness ratios or f_c of concrete infill. Besides, a design approach with the capability of accurately estimating the strength enhancements was also proposed and provides more accurate strength predictions in comparison with those obtained based on approaches in the standards or literature. Chen and Chan [26] experimentally investigated octagonal CFST short columns formed using S460 HSS with nominal f_y of 460MPa and normal- or high-strength concrete infill with f_c ranging from 27.9 to 92.1MPa. Observations for the effects of plate width-to-thickness ratios and f_c of concrete infill were similar to those obtained by Fang et al. [25]. It was found that the design approach in GB 50936-2014 [27] and that suggested by Zhu and Chan [12] can be applied to generate strength predictions for safe design. Although these systematic studies have been conducted for octagonal CFST short columns fabricated with high-strength materials, the research on the behaviour of the structures subjected to combined compression and bending as the typical loading condition for various structural applications [22, 28, 29] remains unexplored and is necessary for safe and economical designs of the structures.

This study is carried out with the aim to investigate the structural performance of high-strength octagonal CFST short columns under combined compression and bending. Experiments were performed on 12 short column specimens with different plate width-to-thickness ratios and subjected to various combinations of compression and bending. Furthermore, numerical simulation was also performed using a validated finite element model. Parametric studies were carried out on high-strength

82 octagonal CFST short columns with a wide range of cross-sectional dimensions and material strengths
83 under combined compression and bending. Based on the experimental and numerical results, the
84 applicability of specifications in the European, Australian and North American standards [30-32] for
85 predicting the strengths of the structures was assessed and the accuracy of the design approaches in
86 the standards was compared and discussed to reduce the conservatism of strength predictions for
87 economical designs.

88 **2. Test program**

89 **2.1 Specimens and material properties**

90 Twelve high-strength octagonal CFST specimens were prepared for the experimental investigation, as
91 summarized in Table 1 based on the nomenclature described in Fig. 1. The specimens are labelled
92 based on the nominal cross-sectional sizes and eccentricities for the compressive loading. For example,
93 the label of Oct-50×6-e20 defines the specimen with the nominal edge length (B) and plate thickness
94 (t) of 50mm and 6mm respectively and tested under combined compression and bending with nominal
95 loading eccentricity of 20mm. The B is counted based on the middle of the outer side of corner regions.
96 For the repeated test, a letter "R" is shown in the label. For the specimens, the outer cold-formed
97 octagonal HSS tubes were fabricated using 6mm thick S690 HSS plates through press-braking into
98 half-sections and subsequent welding of half-sections [25, 33]. Two nominal sectional sizes for the
99 tubes were used with the nominal B as 50mm and 70mm while the measured dimensions, outer corner
100 radius (R_o) and length (L) of the tubes are given in Table 1. Each cold-formed HSS octagonal tube was
101 welded with two 25mm thick end-plates to the ends of the tube. Subsequently, HSC with the grade of
102 C90 was produced using the mix proportion given in Table 2 and poured into the tubes through the
103 openings of the top end-plates. This arrangement for specimen preparation was adopted to avoid the
104 possible cracking of HSC infill due to the welding of end-plates if the HSC was poured in advance.
105 Besides, casting HSC through the holes until filling the holes in end-plates can also preclude possible
106 gaps between the infill and endplates for efficient loading transferred to both outer steel tubes and HSC
107 infill. These specimen preparation processes were considered to ensure the high quality and reliability
108 of experimental investigations based on the consistent and reliable results obtained in the previous

study on octagonal CFST short columns under concentric compression [25]. In parallel to the process of concrete pouring for the short column specimens, 9 cylinder specimens with the standard size of 150×300 mm were also prepared for measuring the f_c of the HSC at the time of testing the short column specimens. Both the cylinder and short column specimens were cured under the ambient condition for more than 28 days before they were tested.

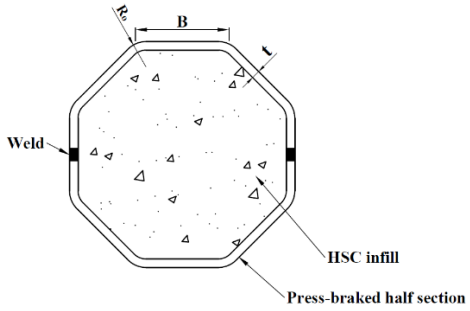

Fig. 1. Cross-section of high-strength octagonal CFST specimens.

Table 1. Geometric properties of high-strength octagonal CFST test specimens.

Specimen	Edge length B (mm)	Thickness t (mm)	Outer corner radius R_o (mm)	Length L (mm)	e_0 (mm)	Effective length L_{eff} (mm)
Oct-50×6-e10	54.0	6.11	17.0	249.9	10.8	547.9
Oct-50×6-e20	49.9	6.07	18.0	249.6	20.3	547.6
Oct-50×6-e40	51.1	6.12	17.8	249.0	40.4	547.0
Oct-50×6-e60	50.5	6.12	18.0	248.8	59.9	546.8
Oct-50×6-e75	49.5	6.13	17.5	249.0	76.1	547.0
Oct-50×6-e90	50.3	6.11	18.0	249.2	90.1	547.2
Oct-70×6-e20	68.7	6.00	17.5	398.1	20.8	696.1
Oct-70×6-e35	68.8	6.01	18.0	398.0	35.5	696.0
Oct-70×6-e60	65.4	6.02	18.0	399.8	60.1	697.8
Oct-70×6-e60R	65.4	6.03	17.5	397.9	60.9	695.9
Oct-70×6-e75	68.0	6.10	17.0	399.0	75.6	697.0
Oct-70×6-e90	66.5	6.05	18.0	400.0	91.2	698.0

Table 2. Mix proportions of C90 concrete per m^3 and the average f_c from measurements on nine cylinder specimens.

Concrete grade	Water (kg)	Cement (kg)	Sand (kg)	10mm aggregate (kg)	20mm aggregate (kg)	Superplasticizer (kg)	f_c (MPa) at the time of testing
C90	128	510	510	423	635	15	104.2 (CoV of 0.04)

The material properties of the outer cold-formed octagonal HSS tubes and the HSC infill were also measured. Tensile coupon specimens were extracted from the flat and corner regions of the tubes and tested with detailed procedures and results reported in the previous studies [25, 33] using the tubes fabricated in the same batch. Thus, only key results of the measured material properties are introduced in this study. The average material properties from the measurements are summarized in Table 3, where E_s, $\sigma_{0.2}$, σ_u, ε_u and ε_f represent the elastic modulus, 0.2% proof stress, ultimate tensile strength, ultimate tensile strain, and elongation at fracture, respectively. As can be seen in the table, the materials at the corner regions demonstrate higher ultimate strength but lower ductility than those of the materials at the flat regions due to the cold-working effect caused by the press-braking fabrication. This observation agrees with those obtained for cold-formed steel circular and rectangular tubular members which are widely applied in structural designs and construction [18]. For the HSC infill, the cylinder specimens were tested during the period of testing the high-strength octagonal CFST short column specimens [34]. The measured f_c varies between 100.15 MPa and 112.63 MPa with CoV of 0.04 and the average f_c is 104.2MPa, as shown in Table 2. Based on the f_c, the elastic modulus of the HSC infill can be estimated for structural analysis and design [25].

Table 3. Average flat and corner material properties measured for cold-formed octagonal HSS tubes [25, 33].

Cross-sectional region	E_s (GPa)	$\sigma_{0.2}$ (MPa)	σ_u (MPa)	ε_u (%)	ε_f (%)
Flat	214	758	801	4.5	13.8
Corner	198	783	845	1.3	11.6

2.2 Tests on specimens under combined compression and bending

The high-strength octagonal CFST short column specimens were tested under eccentric compression providing the combined compression and bending condition. The tests were conducted using a 5000kN capacity Instron testing machine, as shown in Fig. 2 for the test set-up. The knife edges and wedge plates connected to the specimen with high-strength bolts were used to obtain the pin-ended conditions. The effective length (L_{eff}) of each specimen is the vertical distance between the top and bottom knife edges and shown in Table 1. Slot holes grooved on each wedge plate were used to accommodate loading eccentricities by offsetting the centreline of each specimen from the loading line. The initial

loading eccentricity (e_0) was the same at the top and bottom to generate uniform end moments. Various values for e_0 up to about 90mm were applied in order to obtain a wide range of bending-to-compression ratios. The e_0 for the specimens with B of 50mm and 70mm are about the same. The e_0 of 10mm was not used for testing the specimens with B of 70mm to avoid the possibility of having an ultimate load higher than 4500kN which is the upper limit for safely testing with the machine. The Oct-70×6-e60R is a repeated specimen tested using the e_0 of 60mm to confirm the reliability of the experimental investigation. The actual value of e_0 in each test between the centre of the specimen and the middle of the knife edges was measured using a total station based on the space coordinates [33].

Furthermore, three linear variable displacement transducers (LVDTs) with two located at the back and one in front were used to measure axial displacements. One LVDT was also placed at mid-height of each specimen to measure the lateral deflection. Besides, strain gauges were attached to the surfaces of the outer tubes at mid-height to measure the longitudinal strains at these locations. During each test, the specimen was loaded based on the displacement control at the rate of 0.25mm/min so that the structural performance of the specimen in the post-ultimate stage can also be observed.

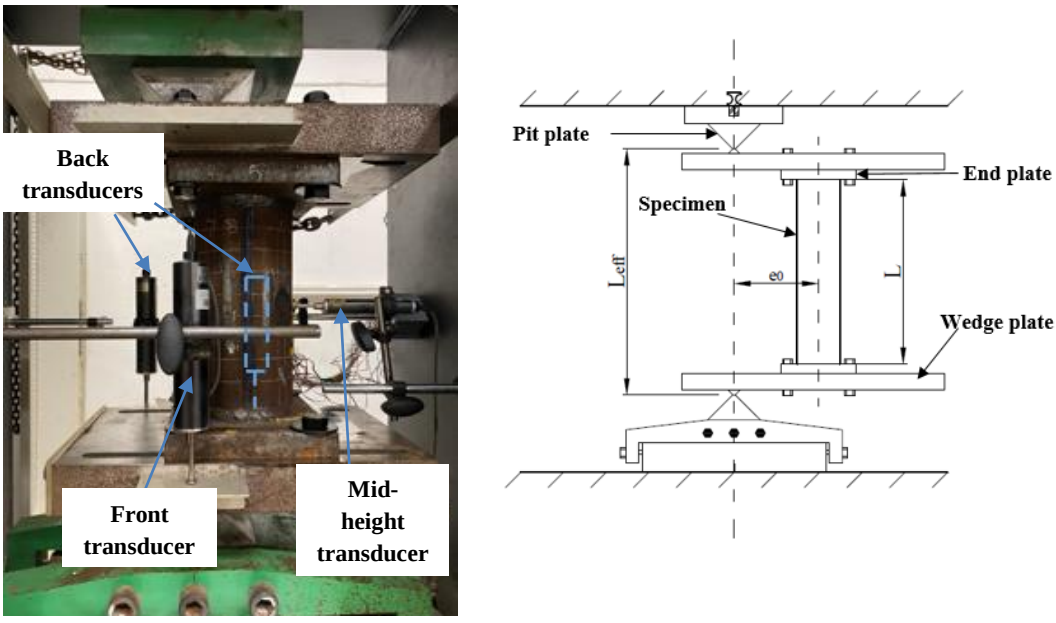

Fig. 2. Test set-up.

2.3 Test results

From the testing on the high-strength octagonal CFST specimens, the load - axial shortening and load – mid height deflection relationships were obtained and are plotted in Figs. 3 and 4 respectively. As

can be seen in the figures, the initial increment of loads with axial shortening or mid-height deflection is linear. After the loads reached about 70% of the ultimate loads ($N_{u,exp}$), the loads increased gradually with the rate lower than that for the increment of axial shortening or mid-height deflection. For specimens with the same nominal cross-sectional size, the $N_{u,exp}$ and initial stiffness reduced with increasing e_0 due to the increasing end moments. Besides, the load - axial shortening and load – mid height deflection relationships obtained for the Oct-70×6-e60R almost coincide with those obtained for the Oct-70×6-e60, revealing the excellent reliability and quite low deviation of the test results. Based on these results, the $N_{u,exp}$ for the short columns were also obtained, as summarized in Table 4. The moment ($M_{u,exp}$) corresponding to the $N_{u,exp}$ was also estimated based on the actual values of e_0 and measured mid-height deflection. In addition, it can be observed that the specimens with B of 70mm demonstrate lower ductility compared with the specimens with B of 50mm due to the higher plate width-to-thickness ratios, which leads to lower steel ratios and reduced confinement effects that can influence the deformation capacity of CFST structures [3, 25].

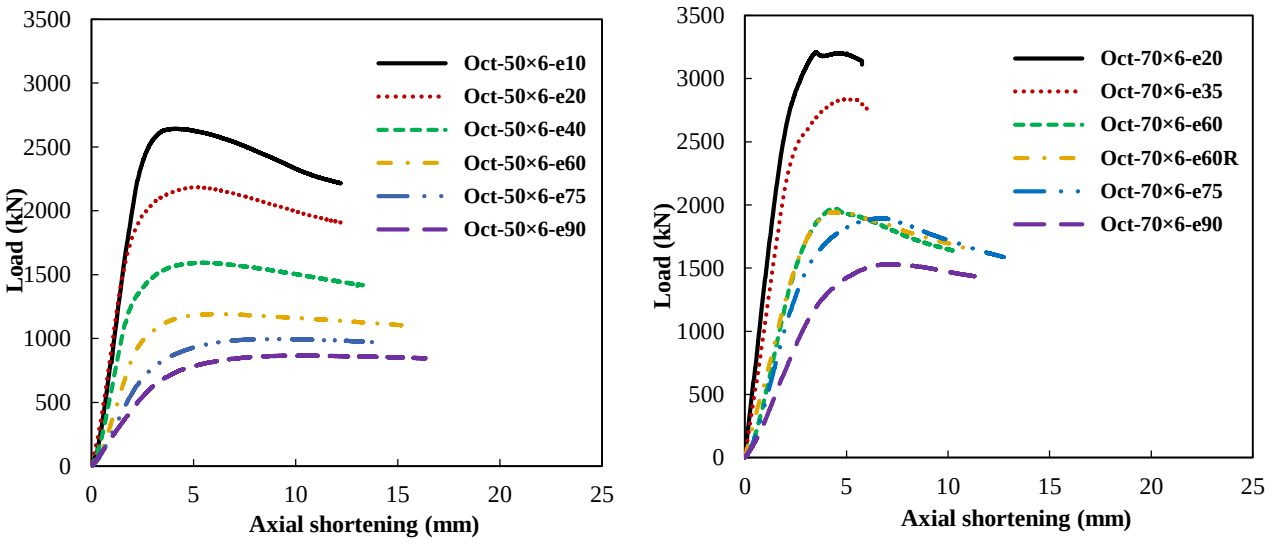

(a)Oct-50×6 specimens (b) Oct-70×6 specimens

Fig. 3. Load versus axial-shortening curves obtained for different test specimens.

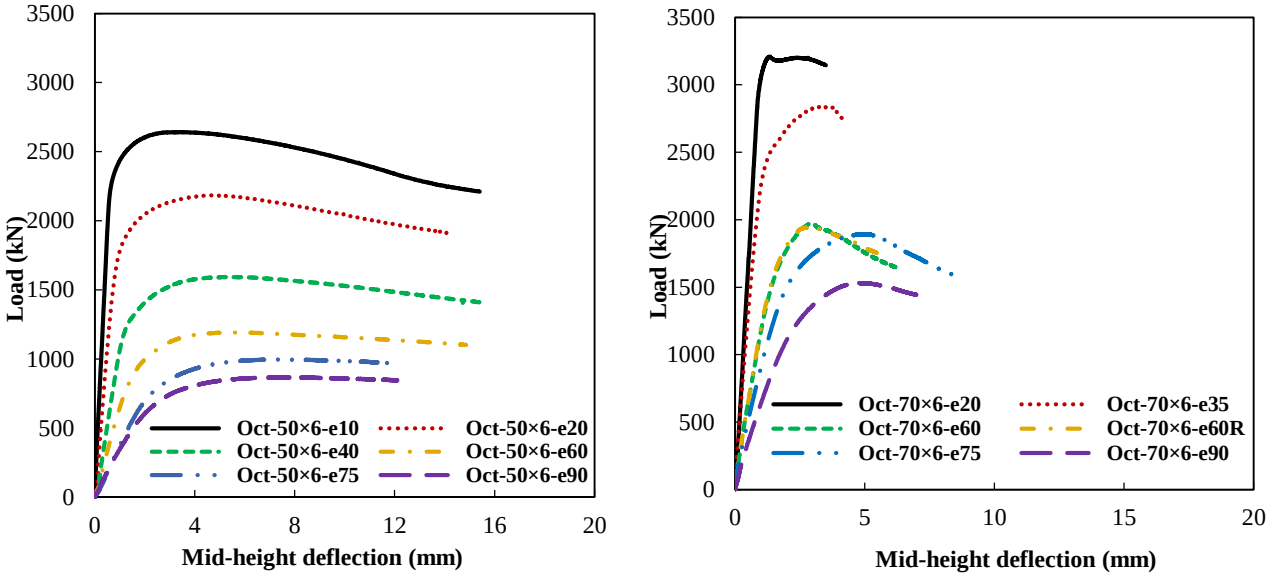

(a)Oct-50×6 specimens (b) Oct-70×6 specimens

Fig. 4. Load versus mid-height deflection curves obtained for different test specimens.

Table 4. Experimental and FE results on high-strength octagonal CFST test specimens.

Section	$N_{u,exp}$ (kN)	$M_{u,exp}$ (kNm)	$N_{u,FE}$ (kN)	$M_{u,FE}$ (kNm)	$N_{u,FE}/N_{u,exp}$	$M_{u,FE}/M_{u,exp}$
Oct-50×6-e10	2641.4	37.5	2687.1	37.1	1.02	0.99
Oct-50×6-e20	2184.0	54.7	2125.4	56.5	0.97	1.03
Oct-50×6-e40	1592.8	72.6	1560.3	70.4	0.98	0.97
Oct-50×6-e60	1191.4	78.2	1170.9	78.2	0.98	0.99
Oct-50×6-e75	996.0	83.0	959.9	78.6	0.96	0.95
Oct-50×6-e90	866.1	84.1	839.5	81.4	0.97	0.97
Oct-70×6-e20	3208.7	70.8	3321.1	76.6	1.04	1.08
Oct-70×6-e35	2836.7	110.2	2921.2	119.0	1.03	1.08
Oct-70×6-e60	1974.5	124.4	1938.9	128.0	0.98	1.02
Oct-70×6-e60R	1945.9	124.0	1922.1	128.1	0.99	1.03
Oct-70×6-e75	1895.1	153.0	1922.5	157.7	1.01	1.03
Oct-70×6-e90	1531.9	147.4	1549.5	152.1	1.01	1.03
				Mean	1.00	1.01
				CoV	0.02	0.04

The load versus mid-height longitudinal strains responses were also measured and the results are presented in Fig. 5 for typical specimens. For Oct-50×6-e10 and Oct-70×6-e20 specimens under the loading with relatively lower e_0, the compressive strains with negative values were observed in the initial loading stage, demonstrating that the specimens were mainly under compression due to the relatively lower end moments. After the $N_{u,exp}$ were reached for the specimens, the tensile strains from strain gauges SG3 attached on the tension side of the specimens were observed due to the larger moments with increasing mid-height deflection. For the specimens tested under higher e_0 values,

tensile strains from SG3 strain gauges were obtained and are higher in the ascending path under the same load with increasing e_0 due to the increasing moments acting on the specimens [35], as observed in Figs. 5(a) and (b). These observations of the strains from the compression and tension sides of specimens can support the evaluation of design approaches based on the stress distribution with increasing bending moment exerted on the structures, as discussed in Section 4.1.

Further to these load versus displacement or strain responses, the failure modes of the specimens were also observed from the tests. For all the short column specimens, the observed failure was the outward local buckling of the outer octagonal HSS tubes due to the prevention of inward buckling with concrete-infill, and the crushing of concrete infill due to the higher strains than that for concrete failure under compression. Typical specimens after testing are shown in Fig. 6 for the failure modes. The observations of inelastic local buckling near the ends of some specimens may be caused by the combined effect of relatively large local imperfections caused by the welding of end plates at the two ends of each HSS octagonal tube, and the high stress concentration at these locations when the applied loading was transferred to the specimen ends.

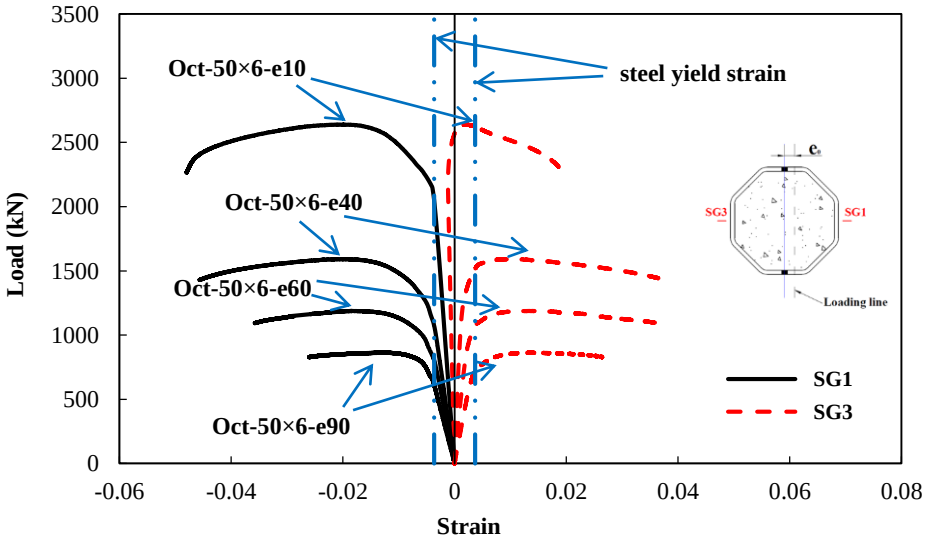

(a) Oct-50×6 specimens

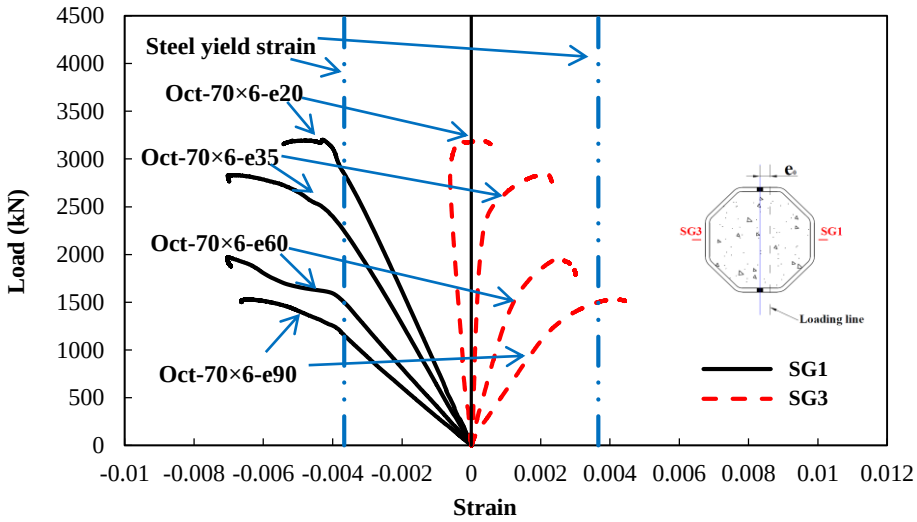

(b) Oct-70×6 specimens

Fig. 5. Load versus longitudinal strains for typical test specimens.

Fig. 6. Failure modes of typical test specimens.

3. Finite element modelling

Supplementary to the experimental testing, numerical simulation through finite element modelling was carried out to investigate the structural performance of high-strength octagonal CFST short columns with a wide range of parameters and under combined compression and bending. The finite element (FE) model developed using the ABAQUS 6.14 software package [36], model validation and parametric studies are presented in the following sections.

3.1 Description of the finite element model

To simulate the high-strength octagonal CFST short columns, S4R shell elements were adopted to model the outer octagonal HSS tubes [14, 38] while the C3D8R solid elements were used for the HSC infill [25, 37]. The element mesh size of about *B*/8 was applied to the outer tubes and HSC infill based

on the mesh convergence study. The interaction between the outer octagonal HSS tubes and HSC infill was simulated using the surface-to-surface contact. In the normal direction, the hard contact was employed. In the tangential direction, the Coulomb friction model was applied with the friction coefficient taken as 0.25 [25, 39].

The material properties input for the outer octagonal HSS tubes were based on the measured properties for the tubes, as shown in Table 3. The measured stress-strain relationship reported in Fang et al. [25] for the material was converted into the true stress - true plastic strain relationship that was incorporated in the FE model. To simulate the properties of the HSC infill, the concrete damage plasticity model based on the mathematical constitutive model developed and validated with the capability of simulating the behaviour of concrete [35, 40-41] was used in this study. For the properties of HSC infill in the elastic stage, the elastic modulus (E_c) was taken as $4700 \times f_c^{0.5}$ [6, 25] while the Poisson's ratio equals to 0.2. To take into account the confinement effect in CFST structures [22, 35], the constitutive model suggested by Han et al. [42] for circular CFSTs was used to estimate the stress-strain relationship for the HSC infill since it was found to generate accurate FE predictions for high-strength octagonal CFST short columns under concentric compression in the previous study [25]. Its suitability for simulating the structures subjected to combined compression and bending was further calibrated in this study through FE model validation. Besides, other parameters required for the concrete damage plasticity model include the dilation angle (φ), flow potential eccentricity (e), the ratio of the compressive strength under biaxial loading to uniaxial compressive strength (f_{b0}/f_{ck}), the ratio of the second stress invariant on the tensile meridian to that on the compressive meridian (K_c) and viscosity parameter. The φ was estimated using Eqs. (1) and (2) provided in Tao et al. [43]. In the equations, the A_s and A_c are the cross-sectional area for the outer steel tube and concrete infill, respectively. For e and viscosity parameter, default values of 0.1 and 0 respectively were adopted. The f_{b0}/f_{ck} was estimated using Eq. (3) given by Papanikolaou and Kappos [44] while the K_c was obtained based on Eq. (4) from Tao et al. [43] and Yu et al. [45]. The tensile properties of the HSC infill also need to be defined in the model and were incorporated with the tensile strength as $0.1\times f_c$ and the

fracture energy (G_f) estimated from Eq. (5) [43]. The d_{max} in Eq. (5) refers to the maximum coarse aggregate size in mm and was 20mm for the HSC infill in this study.

$$\Psi = \begin{cases} 56.3 \times (1-\xi) & for\ \xi \le 0.5 \\ 6.672 \times e^{\frac{7.4}{4.64+\xi}} & for\ \xi > 0.5 \end{cases} \quad (1)$$

$$\xi = \frac{A_s f_y}{A_c f_c} \quad (2)$$

$$f_{b0}/f_{ck} = 1.5/f_c^{0.075} \quad (3)$$

$$K_c = \frac{5.5}{5+2f_c^{0.075}} \quad (4)$$

$$G_F = (0.0469 d_{max}^2 - 0.5 d_{max} + 26)\left(\frac{f_c}{10}\right)^{0.7} \quad (5)$$

Residual stresses and local geometric imperfections were investigated for octagonal HSS tubes and may influence the resistance of HSS octagonal hollow section structures [33, 46]. For the structures with concrete infill, the effect of residual stresses on the structural performance was negligible [25, 47] and thus was not considered in the current study. As for the incorporation of local geometric imperfections, the pattern as the lowest eigenmode shape obtained from the separate eigenvalue buckling analysis was scaled by the local geometric imperfection magnitudes that can be estimated using Eq. (6) for HSS octagonal tubes in [33, 48]. In Eq. (6), ω is the geometric imperfection while the f_{cr} is the elastic buckling stress for the plate with the highest slenderness in a cross section [48]. Boundary conditions for the high-strength octagonal CFST short columns were defined using reference points coupled with the end surfaces of each short column and located offset with the loading eccentricities. At the reference points, the pin-ended boundary conditions were applied. A typical FE model created for the simulation of high-strength octagonal CFST short columns under combined compression and bending is presented in Fig. 7. The loading on each structure was applied by specifying the displacement rate at the reference point on the loaded side in a Static step for predicting the structural performance.

$$\omega = 0.307 t \left(\frac{\sigma_{0.2}}{f_{cr}}\right)^{0.5} \quad (6)$$

3.2 Validation of the FE model

The FE model described earlier in this paper was validated by comparing the FE predictions with test results for the short column specimens involved in the experimental investigations. The FE results for the ultimate loads ($N_{u,FE}$) and the corresponding maximum moments ($M_{u,FE}$) were first compared with the test results, as shown in Table 4. From the table, it can be observed that the $N_{u,FE}$ and $M_{u,FE}$ accorded well with the $N_{u,exp}$ and $M_{u,exp}$ for the high-strength octagonal CFST short columns subjected to different combinations of compression and bending. The mean $N_{u,FE}/N_{u,exp}$ ratio is 1.00 with the coefficient of variation (CoV) of 0.02 and the mean $M_{u,FE}/M_{u,exp}$ ratio equals to 1.01 with the CoV of 0.04.

The load versus mid-height deflection responses predicted through FE modelling for the high-strength octagonal CFST short columns were also compared with those obtained in the tests, as presented in Fig. 8. It can be observed in the figure that the load versus mid-height deflection responses were quite accurately predicted using the FE model. Furthermore, the failure modes of the structures were also replicated in the FE modelling, as demonstrated in Fig. 9. Based on these comparisons between the FE predictions and test results, the FE model is validated with the capability of accurately predicting the behaviour of the high-strength octagonal CFST short columns under combined compression and bending.

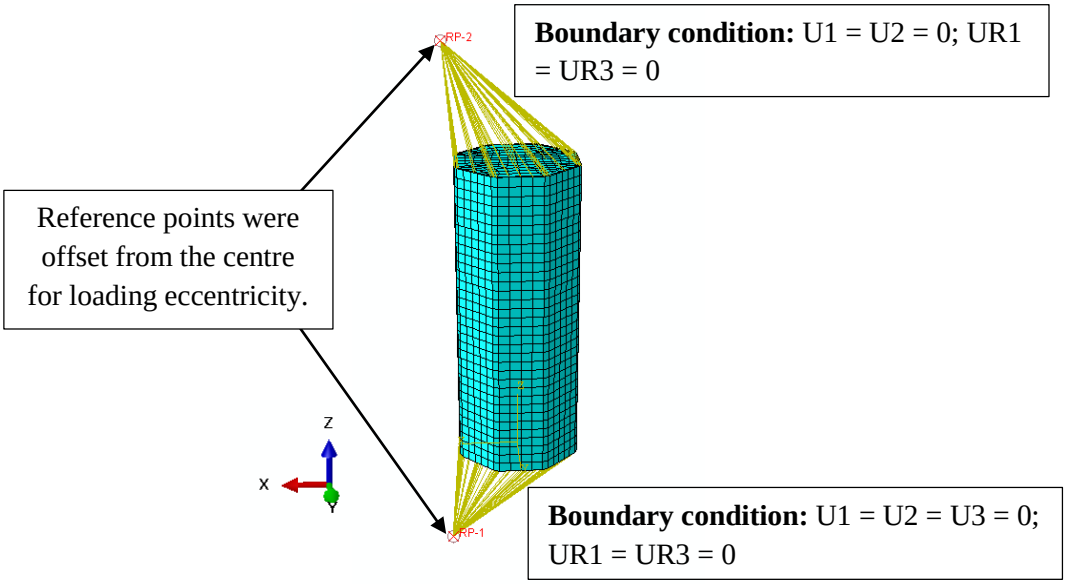

Fig. 7. A typical FE model created for the simulation of high-strength octagonal CFST short columns under combined compression and bending.

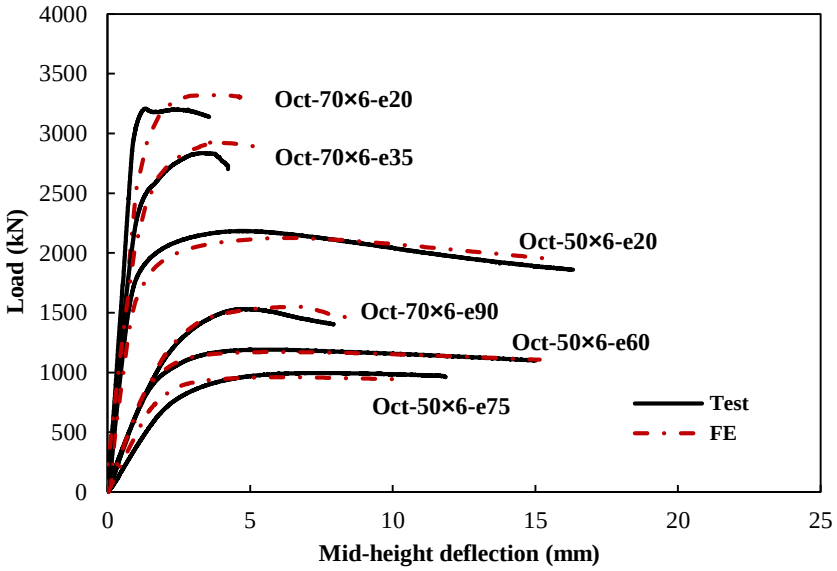

Fig. 8. Comparison of load versus mid-height deflection responses predicted by FE modelling with test results for typical high-strength octagonal CFST short columns under combined compression and bending.

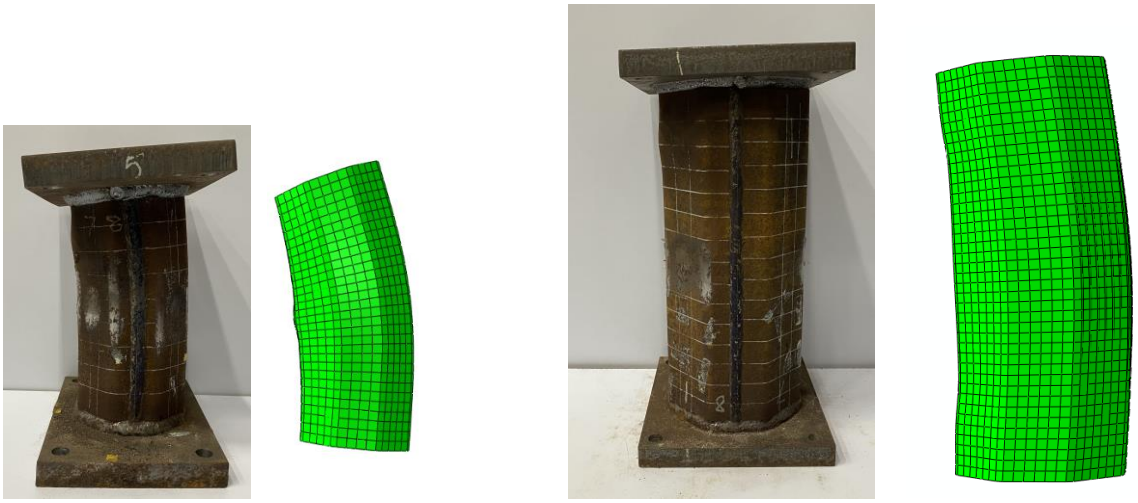

(a) (b)

Fig. 9. Comparison of failure mode predicted by FE modelling with the test result for (a) Oct-50×6-e60 and (b) Oct-70×6-e35.

3.3 Parametric studies

By taking advantage of the validated FE model, parametric studies were carried out to investigate the behaviour of high-strength octagonal CFST short columns with a wide range of cross-sectional dimensions and strengths of HSS octagonal tubes (steel grades) and HSC infill (HSC grades) and under various combinations of compression and bending. The results of parametric studies can also enhance the data that are necessary for evaluating the design approaches to generate reliable design for the structures under combined compression and bending. For the high-strength octagonal CFST short

columns considered in the parametric studies, the width (B) of the outer octagonal tubes was taken as 70mm and the L_{eff} of the structures equals to 700mm. Different values of t between 4.5mm and 8.75mm were used for the outer octagonal tubes in order to consider varying plate width-to-thickness ratios (8.0, 12.06 and 15.56) and investigate their effects on the structural performance of high-strength octagonal CFST short columns. Besides, S460 and S690 HSS were considered since the material properties of octagonal tubes fabricated with these HSS grades were measured and can be used in the parametric studies [25, 33, 49]. Furthermore, HSC infill grades as C70, C100 and C120 with nominal f_c of 70MPa, 100MPa and 120MPa were also considered. A summary of the range of parameters considered for the high-strength octagonal CFST short columns in the parametric studies is presented in Table 5. In order to cover various combinations of compression and bending, ten loading eccentricities ranging from 0mm to 400mm were applied for each high-strength octagonal CFST short column.

Table 5. Range of parameters for geometric and material properties of high-strength octagonal CFST short columns considered in parametric studies.

B (mm)	t (mm)	HSS grades	f_c of HSC infill (MPa)	ξ
70	4.5, 5.8, 8.75	S460, S690	70, 100, 120	0.56-2.65

Based on the parametric study results, the effects of different parameters on the behaviour of high-strength octagonal CFST short columns under combined compression and bending can be observed. Fig. 10 shows the effect of steel grade on the structural performance of the short columns. As can be seen in Fig. 10(a) that shows the compressive load versus moment curves, under the same loading eccentricity, the structural resistance against combined compression and bending increased significantly with increasing steel grades. Typical load versus mid-height deflection responses for the short columns are also presented in Fig. 10(b). It can be observed from Fig. 10(b) that the ultimate loads increase with increasing steel grade for the outer HSS octagonal tubes since more strength contribution can be obtained from the outer tubes with the higher HSS grade [22, 35]. The influence on the flexural stiffness is minimal since the elastic modulus of the outer octagonal tubes remains the same. In addition, the effect of the B/t ratio on the compressive load versus moment curves is presented in Figs. 11(a) and 12(a) for the short columns with S460 and S690 octagonal outer tubes respectively.

It can be observed in the figures that the curves for the high-strength octagonal CFST short columns enlarge with decreasing B/t ratios. The structures with relatively lower B/t ratios demonstrate the higher resistance against combined compression and bending. The increment in resistance for those high-strength octagonal CFST short columns can also be observed in Figs. 11(b) and 12(b) showing the load-mid-height deflection responses of the short columns. Besides, the flexural stiffness also increases with decreasing B/t ratios, as shown in Figs. 11(b) and 12(b). The higher resistance and flexural stiffness obtained with decreasing B/t ratios are due to the increasing structural strength and stiffness contribution from the outer octagonal steel tubes with increasing steel ratios [22, 35, 50-51].

Furthermore, the influence of the HSC infill grade was also investigated based on the parametric study results, as shown in Figs. 13 and 14 for the short columns with S460 and S690 octagonal outer tubes respectively. As can be seen in the figures, the structural resistance of the high-strength octagonal CFST short columns increased with increasing grades of the HSC infill. The resistance increment is more obvious when the compressive loads are higher under relatively lower loading eccentricities since larger proportion of HSC infill is under compression and generates more strength contributions. In addition to the effect of HSC infill grade on structural resistance, the flexural stiffness increment is quite low, as revealed in Figs. 13(b) and 14(b). The low influence on flexural stiffness is due to the very high stiffness contribution from the HSS outer tubes of the short columns with high steel ratios and relatively lower stiffness of the HSC infill than that of HSS tubes. Further to these observations of effects from different parameters, these resultant compressive load versus moment curves demonstrate the variation pattern of compression resistance with increasing bending moment, which should be reflected in the design approaches to generate accurate designs of the structures.

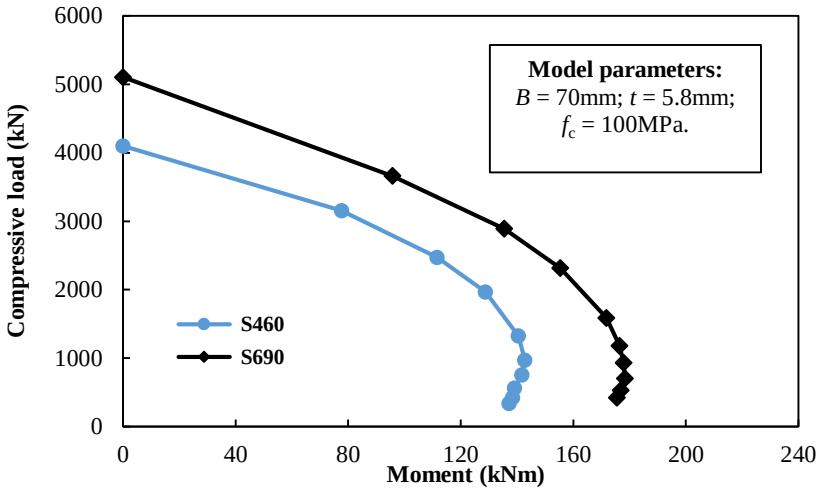

(a)

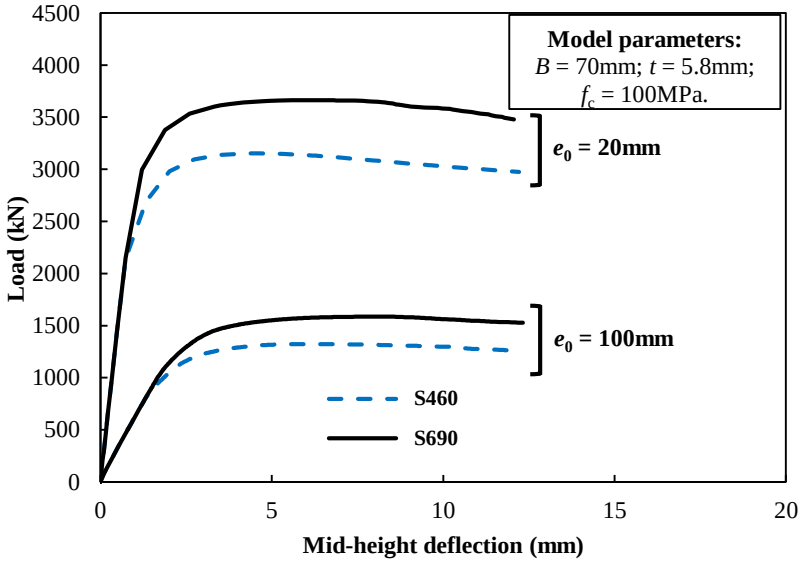

(b)

Fig. 10. Effect of the HSS grade on the (a) compressive load versus moment curves; and (b) load – mid-height deflection relationship, for high-strength octagonal CFST short columns.

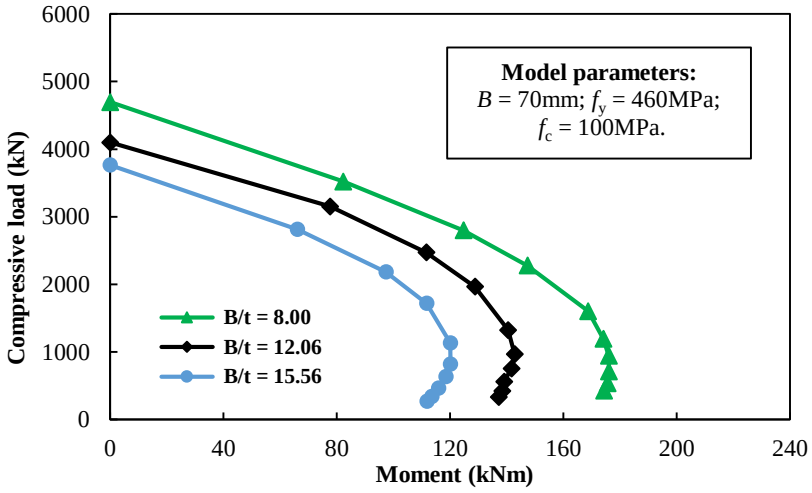

(a)

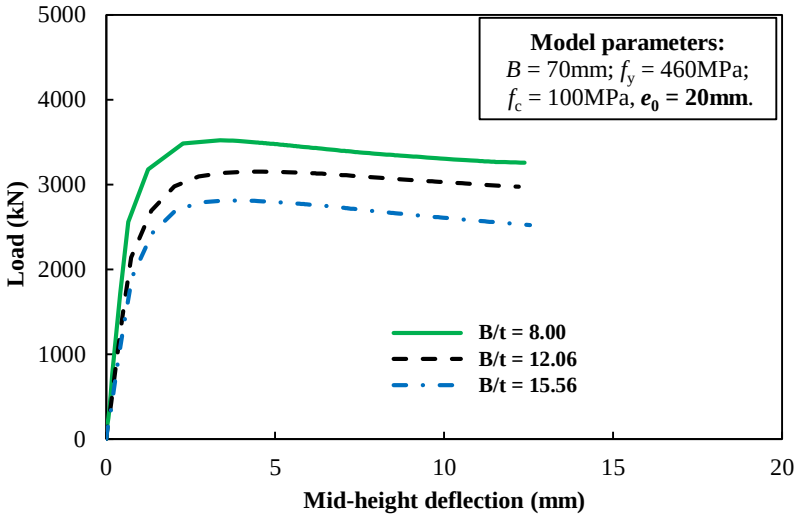

(b)

Fig. 11. Effect of the plate width-to-thickness ratio on the (a) compressive load versus moment curves; and (b) typical load versus mid-height deflection responses, for high-strength octagonal CFST short columns fabricated with S460 octagonal HSS tubes.

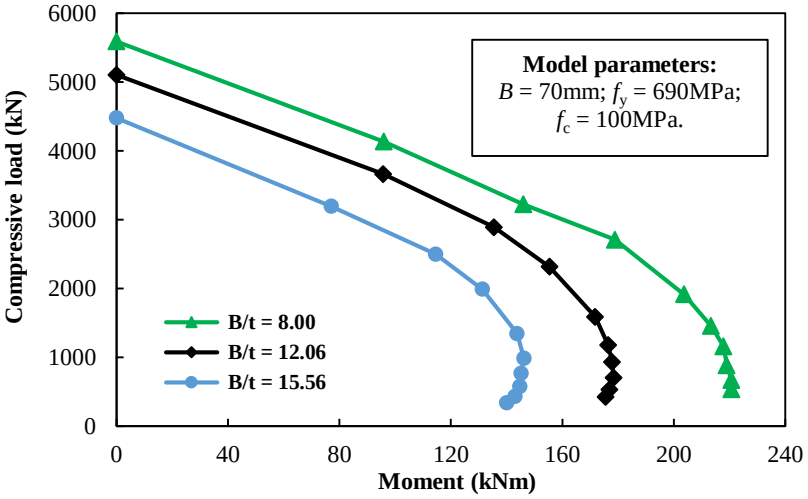

(a)

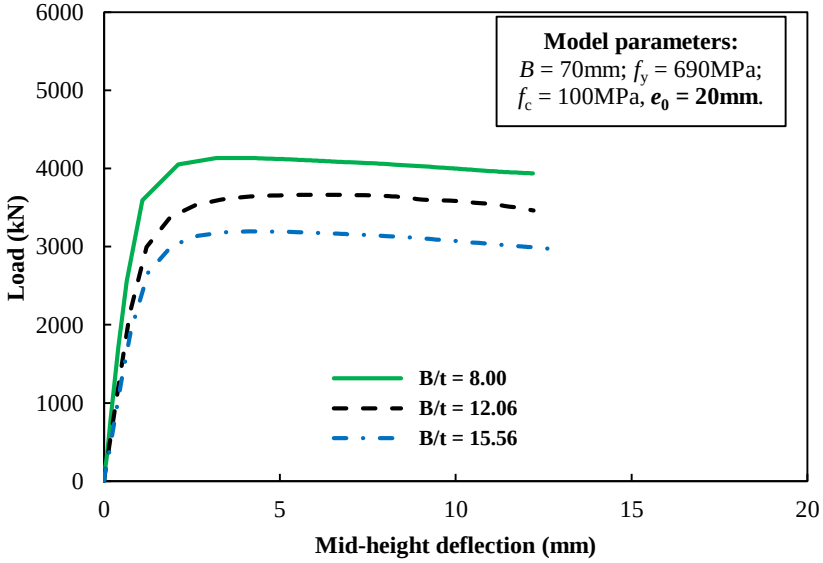

(b)

Fig. 12. Effect of the plate width-to-thickness ratio on the (a) compressive load versus moment curves; and (b) typical load versus mid-height deflection responses, for high-strength octagonal CFST short columns fabricated with S690 octagonal HSS tubes.

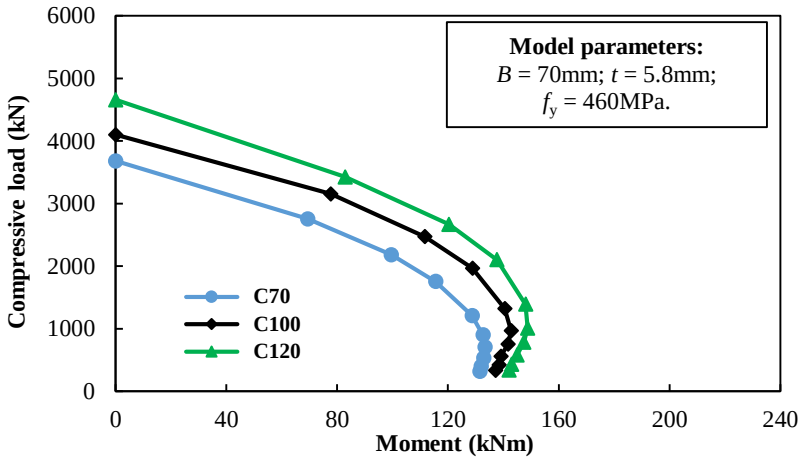

(a)

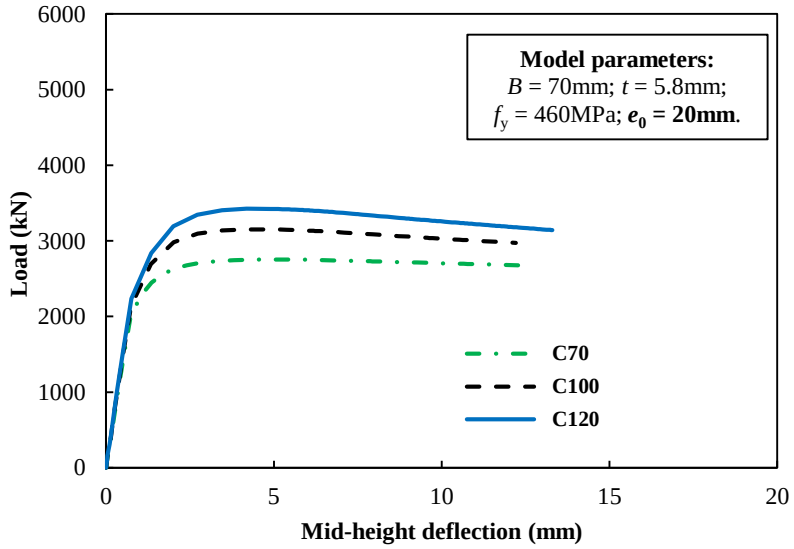

(b)

Fig. 13. Effect of the HSC grade on the (a) compressive load versus moment curves, and (b) typical load versus mid-height deflection responses, for high-strength octagonal CFST short columns fabricated with S460 octagonal HSS tubes.

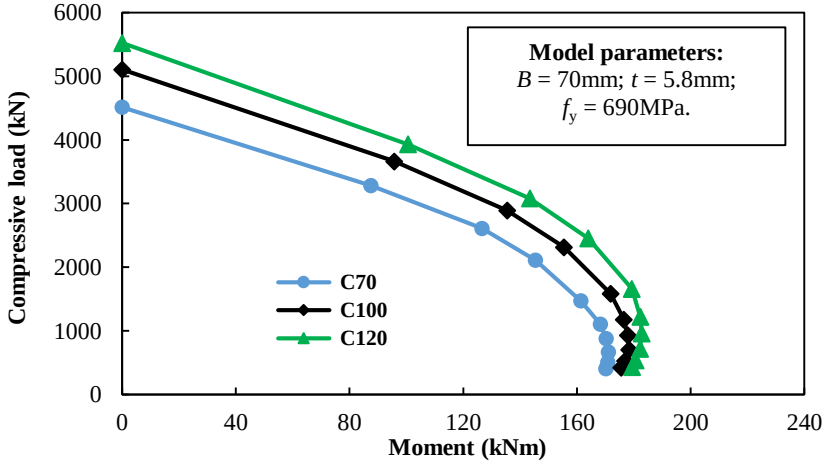

(a)

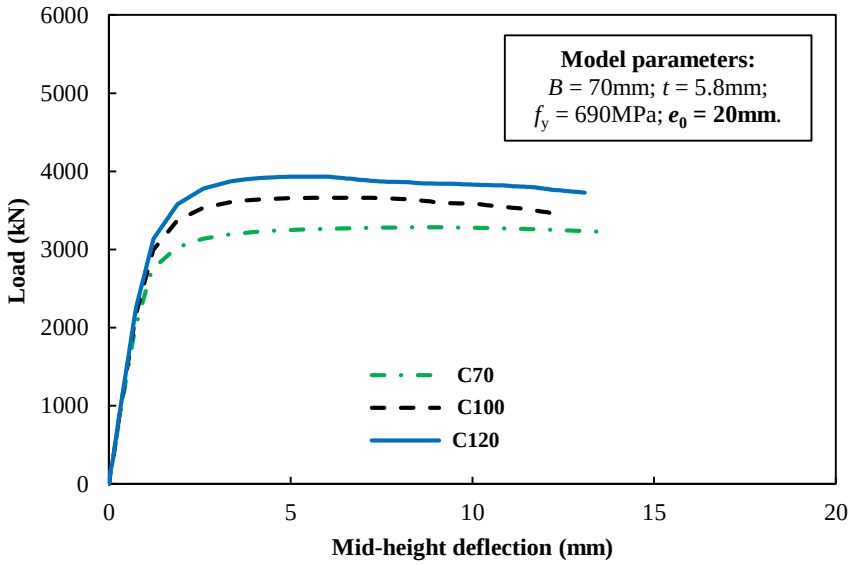

(b)

Fig. 14. Effect of the HSC grade on the (a) compressive load versus moment curves, and (b) typical load versus mid-height deflection responses, for high-strength octagonal CFST short columns fabricated with S690 octagonal HSS tubes.

4. Design approaches

Safe and accurate design approaches are required in order to conduct reliable design for high-strength octagonal CFST structures. The existing design codes have been mainly developed based on CFST structures made of conventional strength materials and their suitability for structures made of high strength materials needs to be evaluated [8, 21, 24]. Besides, existing codes of practice do not cover CFST structural members with the octagonal shaped sections. Thus, in this study, the strengths obtained in the experiments and parametric studies for high-strength octagonal CFST short columns with S460 and S690 HSS, HSC f_c between 70MPa and 120MPa, and B/t ratios from 8.00 to 15.56 (with B between 50 mm and 70 mm) were compared with the strength predictions based on the design approaches in the Eurocode 4, AS 2327 and AISC 360 standards [30-32]. Hence, the applicability of these standards to the structures can be evaluated to form the basis for conducting reliable design of the structures, as described in the subsequent sections.

4.1 Eurocode 4 and AS 2327

Eurocode 4 and AS 2327 provide the same axial load – moment interaction diagrams for predicting the strengths of CFST members subjected to combined compression and bending, as depicted in Fig. 15 (a). Thus, the Eurocode 4 is referred in this study. The interaction diagram describes the variation of ultimate compressive load ($N_{u,EC4}$) of a CFST member under the bending moment of M_{ed}. The

diagram can be obtained based on the change of stress distribution from compressive stress under pure compression to tensile stresses in part of the cross-sections due to the existence of bending moment, as shown in Fig. 15(a). This trend of stress distribution variation agrees with the experimental observation of strain variations, as discussed in Section 2.3, for the high-strength octagonal CFST short columns subjected to different end-moments. To derive the interaction diagrams for high-strength octagonal CFST structures, the N_{us} is the axial compression capacity and the M_{us} is the plastic bending moment capacity which can be estimated based on the plastic stress distribution given for point B in Fig. 15(a). The N_{us} for high-strength octagonal CFST short columns can be conservatively predicted using Eq. (7) provided in the standards for square CFST structures based on the previous research studies [25, 26]. In these studies, approaches are also recommended to obtain more accurate predictions of N_{us} for the structures formed using S460 and S690 HSS octagonal tubes, as given in Eqs. (8) and (9) respectively. The η_{a0} and η_{c0} in Eq. (8) can be estimated using Eqs. (10) and (11) respectively based on the relative member slenderness ($\bar{\lambda}$) specified in the Eurocode 4. The D in Eq. (8) refers to the diameter of the circumcircle for each octagonal cross-section [26]. In order to obtain accurate strength predictions, the Eqs. (8) and (9) were used in this study to estimate N_{us} for the interaction curve. The M_{us} for the interactive diagram can be estimated based on the plastic stress distribution specified in the Eurocode 4 and AS 2327. In the strength predictions, the $\sigma_{0.2}$ for the flat and corner regions was used for the respective areas contributing to the strength of the structures.

$$N_{us,EC4/AS} = \sigma_{0.2} A_s + f_c A_c \tag{7}$$

$$N_{us,S460} = \eta_{a0} \sigma_{0.2} A_s + f_c A_c \left[1 + 0.73 \eta_{c0} \frac{t}{D} \frac{\sigma_{0.2}}{f_c}\right] \tag{8}$$

$$N_{us,S690} = \left[1 - 0.063 ln\left(0.12 \frac{B}{t}\right)\right] \sigma_{0.2} A_s + \left[1 + \left(\frac{t}{B f_c}\right)^{0.35}\right] f_c A_c \tag{9}$$

$$\eta_{a0} = 0.25\left(3 + 2\bar{\lambda}\right) \tag{10}$$

$$\eta_{c0} = 4.9 - 18.5\bar{\lambda} + 17\bar{\lambda}^2 \tag{11}$$

Based on the provisions in these standards, the $N_{u,EC4}$ estimated for the high-strength octagonal CFST short columns are compared with the $N_{u,exp+FE}$ obtained by the testing and numerical parametric studies

for the structures, as shown in Fig. 16 and Table 6 for the statistical evaluation. As can be seen in the figure, the $N_{u,EC4}$ correlate reasonably well with the $N_{u,exp+FE}$, due to the similar pattern of the interaction diagram from Eurocode 4 in comparison with the compressive load – moment curves obtained from parametric studies for the high-strength octagonal CFST short columns. The mean $N_{u,exp+FE}/N_{u,EC4}$ ratio equals to 1.05 with the CoV of 0.05, revealing the conservative strength predictions based on the standards.

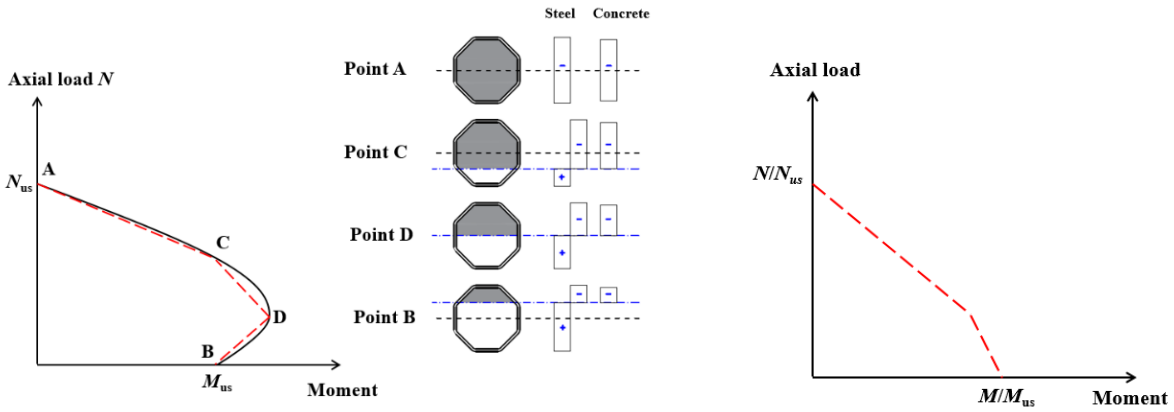

(a) Eurocode 4 & AS2327 (b) AISC 360

Fig. 15. Compression and bending interaction diagrams given in different standards [30-32].

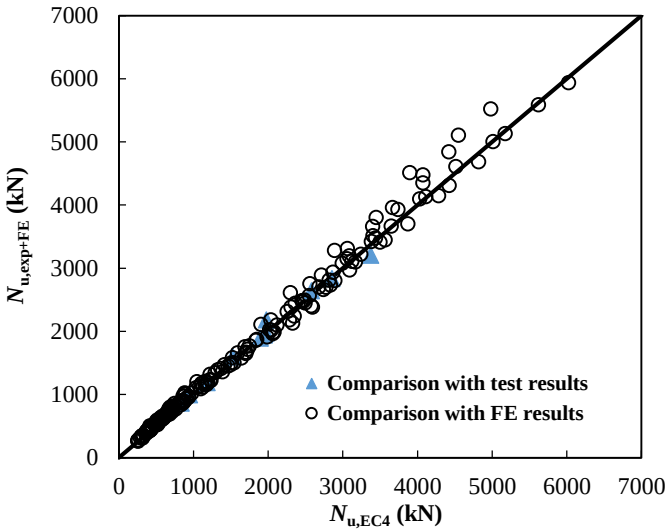

Fig. 16. Comparison of strength predictions based on Eurocode 4 and AS 2327 with the experimental and FE results.

Table 6. Comparison of ultimate loads from experiments and FE parametric studies with strength predictions based on design approaches in standards.

Number of data	Parameters	Eurocode 4 & AS 2327 $N_{u,exp+FE}/N_{u,EC4}$	AISC 360 $N_{u,exp+FE}/N_{u,AISC}$
204	**Mean**	1.05	1.19
	CoV	0.05	0.09

4.2 AISC 360

The AISC 360 standard also provides the axial load – moment interaction diagram for strength predictions of CFSTs under combined loading, as depicted in Fig. 15(b). The diagram can be obtained based on Eq. (12). This interaction diagram is specified for the design of CFST structures with the cross-sections other than rectangular or circular shapes. Other approaches in the standard require the parameters related to rectangular or circular CFSTs and thus are not considered in this study on high-strength octagonal CFST structures. To estimate the N_{us} and M_{us}, the methods for estimating N_{us} and M_{us} introduced in the Section 4.1 of this paper were applied since the design of octagonal CFST structures is not covered in the AISC 360 standard and direct comparison of the interaction diagrams from different standards can also be made.

$$\begin{cases} \frac{N_{u,AISC}}{N_{us}} + \frac{8}{9}\frac{M_{ed,AISC}}{M_{us}} \leq 1, & for\ \frac{N_{u,AISC}}{N_{us}} \geq 0.2 \\ \frac{N_{u,AISC}}{2N_{us}} + \frac{M_{ed,AISC}}{M_{us}} \leq 1, & for\ \frac{N_{u,AISC}}{N_{us}} < 0.2 \end{cases} \quad (12)$$

The accuracy of $N_{u,AISC}$ estimated for the high-strength octagonal CFST short columns was evaluated by comparing with the $N_{u,exp+FE}$ obtained through the testing and parametric studies, as shown in Fig. 17 and Table 6. It can be observed in the figure that the $N_{u,AISC}$ are lower than the $N_{u,exp+FE}$, revealing the conservative strength predictions based on the AISC 360 standard. The mean $N_{u,exp+FE}/N_{u,AISC}$ ratio equals to 1.19 with the CoV of 0.09. Compared with the $N_{u,EC4}$ based on Eurocode 4, more conservative strength predictions were generated using AISC 360 because the strength contribution from concrete for the structures under combined compression and bending was not efficiently considered in the interaction diagram from AISC 360 [8, 52].

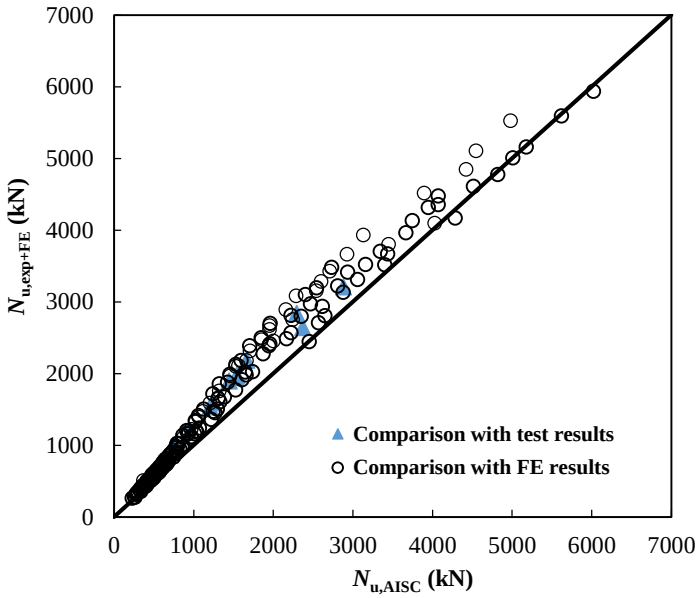

Fig. 17. Comparison of strength predictions based on AISC 360 with the experimental and FE results.

5. Conclusions

The structural performance of high-strength octagonal CFST short columns under combined compression and bending was investigated through testing and numerical modelling. Twelve specimens with different plate width-to-thickness ratios were prepared using S690 HSS octagonal tubes and C90 HSC infill and tested under different combinations of compression and bending. The variation of ultimate loads with increasing end moments due to the higher loading eccentricities applied to the test specimens was observed in the experiments. In addition, numerical modelling was also conducted using a validated FE model on high-strength CFST short columns under combined compression and bending, with the consideration of a wide range of plate width-to-thickness ratios, HSS grades for the outer tubes and HSC infill, to generate sufficient data for the design approach evaluation.

Based on the results obtained from the experiments and numerical modelling, the applicability of design approaches in the Eurocode 4, AS 2327 and AISC 360 standards to high-strength octagonal CFST short columns under combined compression and bending was evaluated. The provisions of axial load versus moment interaction relationship in the Eurocode 4 and AS 2327 standards agree well with the axial compression versus moment variation observed from the experimental and numerical investigations. Thus, the strength predictions based on the Eurocode 4 and AS 2327 standards correlate

quite well with the ultimate loads of the short columns obtained from the results of experiments and numerical modelling and are conservative by 5% on average. Much more conservative strength predictions by 19% on average were obtained using the provisions in the AISC 360 standard, which does not effectively incorporate the strength contribution from concrete for the structures under combined compression and bending. Overall, from the evaluation, these design standards can be safely used for designs of high-strength octagonal CFST short columns under combined compression and bending.

Data Availability Statement

Some or all data that support the findings of this study are available from the corresponding author upon reasonable request.

Acknowledgements

The research work presented in this paper was supported by a grant from the Research Grants Council Research Impact Fund of the Hong Kong Special Administrative Region, China (Project No. R7027-18). The funding support is sincerely appreciated. The authors would also like to sincerely acknowledge the support received from the Chinese National Engineering Research Centre for Steel Construction (Hong Kong Branch) at The Hong Kong Polytechnic University.

References

[1] Li, Y.L., Zhao, X.L., Raman, R.K.SH. and Yu, X. 2018. Axial compression tests on seawater and sea sand concrete-filled double-skin stainless steel circular tubes. *Engineering Structures*, 176, 426-438.

[2] Tran, H., Thai, H.T., Ngo, T., Uy, B., Li, D.X. and Mo, J. 2021. Nonlinear inelastic simulation of high-rise buildings with innovative composite coupling shear walls and CFST columns. *The Structural Design of Tall and Special Buildings*, 30(13), 1-20.

[3] Wang, Z.B., Tao, Z., Han, L.H., Uy, B., Lam, D. and Kang, W.H. 2017. Strength, stiffness, and ductility of concrete-filled steel columns under axial compression. *Engineering Structures*, 135, 209-221.

[4] Al-Attraqchi, A.Y., Hashemi, M.J. and Al-Mahaidi, R. 2020. Hybrid simulation of bridges constructed with concrete-filled steel tube columns subjected to horizontal and vertical ground motions. *Bulletin of Earthquake Engineering*, 18, 4453-4480.

[5] Ahmed, M. and Liang, Q.Q. 2021. Numerical modelling of octagonal concrete-filled steel tubular short columns accounting for confinement effects. *Engineering Structures*, 226, 111405.

[6] Cai, Y.C., Quach, W.M. and Young, B. 2019. Experimental and numerical investigation of concrete-filled hot-finished and cold-formed steel elliptical tubular stub columns. *Thin-Walled Structures*, 145, 106437.

[7] Ding, F.X., Li, Z., Cheng, S.S. and Yu, Z.W. 2016. Composite action of octagonal concrete-filled steel tubular stub columns under axial loading. *Thin-Walled Structures*, 107, 453-461.

[8] Lai, Z.C., Varma, A.H. and Griffis, L.G. 2016. Analysis and design of noncompact and slender CFT beam-columns. *Journal of Structural Engineering*, 142(1), 04015097.

[9] Liao, J.J., Li, Y.L., Ouyang, Y. and Zeng, J.J. 2021. Axial compression tests on elliptical high strength steel tubes filled with self-compacting concrete of different mix proportions. *Journal of Building Engineering*, 40, 102678.

[10] Sheehan, T. Dai, X.H., Chan, T.M. and Lam, D. 2012. Structural response of concrete-filled elliptical steel hollow sections under eccentric compression. *Engineering Structures*, 45, 314-323.

[11] Thai, S., Thai, H.T., Uy, B. and Ngo, T. 2019. Concrete-filled steel tubular columns: test database, design and calibration. *Journal of Constructional Steel Research*, 157, 161-181.

[12] Zhu, J.Y. and Chan, T.M. 2018. Experimental investigation on octagonal concrete filled steel stub columns under uniaxial compression. *Journal of Constructional Steel Research*, 147, 457-467.

[13] Du, Y.S., Chen, Z.H. and Xiong, M.X. 2016. Experimental behavior and design method of rectangular concrete-filled tubular columns using Q460 high-strength steel. *Construction and Building Materials*, 125, 856-872.

[14] Liu, H.X., Fang, H., Zhu, J.Y. and Chan, T.M. 2021. Numerical investigation on the structural performance of octagonal hollow section columns. *Structures*, 34, 3257-3267.

[15] Zhang, Y.B., Han, L.H., Zhou, K. and Yang, S.T. 2019. Mechanical performance of hexagonal multi-cell concrete-filled steel tubular (CFST) stub columns under axial compression. *Thin-Walled Structures*, 134, 71-83.

[16] Fang, H. and Chan, T.M. 2019. Resistance of axially loaded hot-finished S460 and S690 steel square hollow stub columns at elevated temperatures. *Structures*, 17, 66-73.

[17] Su, M.N., Cai, Y.C., Chen, X.R. and Young, B. 2020. Behaviour of concrete-filled cold-formed high strength steel circular stub columns. *Thin-Walled Structures*, 157, 107078.

[18] Fang, H., Chan, T.M. and Young, B. 2018. Structural performance of cold-formed high strength steel tubular columns. *Engineering Structures*, 177, 473-488.

553 [19] Zhang, H.Y., Zhou, X.H., Ke, K., Yam, M.C.H., He, X.Z. and Li, H. 2022. Self-centring hybrid-steel-
554 frames employing energy dissipation sequences: Insights and inelastic seismic demand model. *Journal of*
555 *Building Engineering*, 105451.

556 [20] Song, Y.C., Li, J. and Chen, Y.Y. 2019. Local and post-local buckling of normal/high strength steel sections
557 with concrete infill. *Thin-Walled Structures*, 138, 155-169.

558 [21] Xiong, M.X., Xiong, D.X. and Liew, J.Y.R. 2017a. Axial performance of short concrete filled steel tubes
559 with high- and ultra-high-strength materials. *Engineering Structures*, 136, 494-510.

560 [22] Huang, Z.C., Uy, B., Li, D.X. and Wang, J. 2020. Behaviour and design of ultra-high-strength CFST
561 members subjected to compression and bending. *Journal of Constructional Steel Research*, 175, 106351.

562 [23] Patel, V.I., Hassanein, M.F., Thai, H.T., Al Abadi, H., Elchalakani, M. and Bai, Y. 2019. Ultra-high
563 strength circular short CFST columns: axisymmetric analysis, behavior and design. *Engineering Structures*, 179,
564 268-283.

565 [24] Xiong, M.X., Xiong, D.X. and Liew, J.Y.R. 2017b. Flexural performance of concrete filled tubes with high
566 tensile steel and ultra-high strength concrete. *Journal of Constructional Steel Research*, 132, 191-202.

567 [25] Fang, H., Chan, T.M. and Young, B. 2021a. Structural performance of concrete-filled cold-formed high-
568 strength steel octagonal tubular stub columns. *Engineering Structures*, 239, 112360.

569 [26] Chen, J.B. and Chan, T.M. 2021. Compressive behaviour and design of compact to slender octagonal
570 concrete-filled steel tubular stub columns. *Thin-Walled Structures*, 167, 108211.

571 [27] CABP M. 2014. *Technical Code for Concrete-Filled Steel Tubular Structures* GB 50936-China
572 Architecture & Building Press (CABP), Beijing, China. (in Chinese)

573 [28] Fang, H. and Visintin, P. 2021. Behavior of geopolymer concrete-filled circular steel tube members.
574 *ce/papers*, 4, 593-597.

575 [29] Yazdi, H.A., Hashemi, M.J., Al-Mahaidi, R. and Gad, E. 2021. Multi-axis testing of concrete-filled steel
576 tube columns forming ductile soft-story in multi-story buildings. *Journal of Constructional Steel Research*, 183,
577 106736.

578 [30] ANSI/AISC 360-16, 2016. *Specification for structural steel buildings*. AISC, Chicago.

579 [31] AS/NZS 2327, 2017. *Composite steel-concrete construction for buildings*, Standard Australia/New Zealand.

580 [32] EN1994-1-1, 2004. *Eurocode 4: Design of Composite Steel and Concrete Structures-Part1-1: General*
581 *Rules and Rules for Buildings*, European Committee for Standardization.

[33] Fang, H., Chan, T.M. and Young, B. 2021b. Experimental and numerical investigations of octagonal high-strength steel tubular stub columns under combined compression and bending. *Journal of Structural Engineering*, 147(1), 04020282.

[34] Li, H.T. and Young, B. 2018. Experimental investigation of concrete-filled high-strength steel tubular X joints. *Journal of Structural Engineering*, 144(10), 04018178.

[35] Fang, H. and Visintin, P. 2022. Structural performance of geopolymer-concrete-filled steel tube members subjected to compression and bending. *Journal of Constructional Steel Research*, 188, 107026.

[36] ABAQUS version 6.14. 2014. Dassault Systèmes, Providence, RI.

[37] Deng, R., Zhou, X.H., Deng, X.W., Ke, K., Bai, J.L. and Wang, Y.H. 2021. Compressive behaviour of tapered concrete-filled double skin steel tubular stub columns. *Journal of Constructional Steel Research*, 184, 106771.

[38] Liu, J.Z., Fang, H. and Chan, T.M. 2022. Experimental and numerical investigations on stub column behaviour of cold-formed high strength steel irregular octagonal hollow sections. *Thin-Walled Structures*, 180, 109770.

[39] Debnath, P.P. and Chan, T.M. 2021. Tensile behaviour of headed anchored hollo-bolts in concrete filled hollow steel tube connections. *Engineering Structures*, 234, 111982.

[40] Lee, J. 1996. *Theory and implementation of plastic-damage model for concrete structures under cyclic and dynamic loading*. PhD dissertation, Department of Civil and Environmental Engineering, University of California, Berkeley, California, United States.

[41] Lubliner, J., Oliver, J., Oller, S. and Oñate, E. 1989. A plastic-damage model for concrete. *International Journal of Solids and Structures*, 25(3), 299-326.

[42] Han, L.H., Yao, G.H. and Tao, Z. 2007. Performance of concrete-filled thin-walled steel tubes under pure torsion. *Thin-Walled Structures*, 45, 24-36.

[43] Tao, Z., Wang, Z.B. and Yu, Q. 2013. Finite element modelling of concrete-filled steel stub columns under axial compression. *Journal of Constructional Steel Research*, 89, 121-131.

[44] Papanikolaou, V.K. and Kappos, A.J. 2007. Confinement sensitive plasticity constitutive model for concrete in triaxial compression. *International Journal of Solids and Structures*, 44 (21), 7021-7048.

[45] Yu, T., Teng, J.G., Wong, Y.L. and Dong, S.L. 2010. Finite element modelling of confined concrete I: drucker-Prager type plasticity model. *Engineering Structures*, 32 (3), 665-679.

[46] Chen, J.B., Fang, H. and Chan, T.M. 2021. Design of fixed-ended octagonal shaped steel hollow sections in compression. *Engineering Structures*, 228, 111520.

[47] Wang, F.Y., Young, B. and Gardner, L. 2020. CFDST sections with square stainless steel outer tubes under axial compression: Experimental investigation, numerical modelling and design. *Engineering Structures*, 207, 110189.

[48] Fang, H., Chan, T.M. and Young, B. 2019. Behavior of octagonal high-strength steel tubular stub columns. *Journal of Structural Engineering*, 145(12), 04019150.

[49] Chen, J.B., Zhu, J.Y. and Chan, T.M. 2020. Experimental and numerical investigation on stub column behaviour of cold-formed octagonal hollow sections. *Engineering Structures*, 214, 110669.

[50] Albero, V., Ibañez, C., Piquer, A. and Hernández-Figueirido, D. 2021. Behaviour of slender concrete-filled dual steel tubular columns subjected to eccentric loads. *Journal of Constructional Steel Research*, 176, 106365.

[51] Ahmed, M., Liang, Q.Q., Patel, V.I. and Hadi, M.N.S. 2020. Computational simulation of eccentrically loaded circular thin-walled concrete-filled double steel tubular slender columns. *Engineering Structures*, 213, 110571.

[52] Lai, Z.C., Varma, A.H. and Zhang, K. 2014. Noncompact and slender rectangular CFT members: Experimental database, analysis, and design. *Journal of Constructional Steel Research*, 101, 455-468.